# Dalton Transactions



**PAPER** 

View Article Online
View Journal | View Issue



**Cite this:** *Dalton Trans.*, 2025, **54**, 15062

# Study on a high refractive index sensitivity four-band tunable absorber based on AlCuFe quasicrystals at terahertz frequencies

Wen Gao, Huafeng Zhang, \*\* Mengsi Liu, \* Shubo Cheng\* and Zao Yi \* \*b,c

Optical devices operating in the terahertz band have enormous potential applications, and research in this band is attracting increasing attention from researchers. In this paper, an absorber based on AlCuFe quasicrystals is proposed in the terahertz band, accompanied by four perfect narrow peak absorptions. The bottom layer of the model is gold, mainly serving a reflective function, above the gold is silicon dioxide, with a Dirac semimetal AlCuFe quasicrystal microstructure with hollow spaces around its edges and central region on the top layer. The finite element method is used for simulation calculation, followed by data post-processing and analysis of the device performance. Analysis revealed that this absorber achieved perfect absorption, with absorption rates exceeding 94% at frequencies of 4.99 THz, 6.138 THz, 7.846 THz, and 9.05 THz, with three of these frequencies reaching absorption rates above 97%. The physical mechanism was analyzed in detail using cavity resonance (CR), impedance matching and equivalent circuit theories. The effects of geometrical parameters, electromagnetic wave incidence angle, and the external environment's refractive index on the absorber were thoroughly investigated. The absorber's maximum value of the refractive index sensitivity S was calculated to be 2800 GHz RIU<sup>-1</sup>, indicating high detection accuracy. In the field of detection, the quality factor Q value of an absorber is used to measure its energy loss and high selectivity, while the figure of merit (FOM) value plays a role in evaluating its sensing performance. We calculated the Q value and FOM value, with maximum values of 117.1 and 20.42, respectively, demonstrating that the terahertz perfect absorber proposed in this paper possesses exceptional detection performance.

Received 13th August 2025, Accepted 9th September 2025 DOI: 10.1039/d5dt01929j

rsc.li/dalton

#### 1. Introduction

Terahertz waves (THz, 1 THz =  $10^{12}$  Hz, the photon energy is 4.1 meV) are electromagnetic waves with a specific frequency range between 0.1 THz and 10 THz.<sup>1-3</sup> The material response of electromagnetic devices mainly depends on the frequency of electromagnetic waves. Devices operating at microwave or lower frequencies can be analysed using electronics, while devices operating at infrared and higher frequencies can be analysed using photonics. However, the terahertz band occupies a unique position, located between the infrared band in the optical domain and the millimetre wave band in the microwave domain, at the transition point between electronics and photonics, and thus belongs to the cross-disciplinary field between the two. Due to the many unique properties of tera-

hertz waves, for instance, their high transmittance and resolution, unique coherence, low energy, and transient and broadband characteristics, they stand out significantly compared to electromagnetic waves, <sup>4</sup> and they show great potential in fields such as biomedical detection, radar imaging, material identification, biosensing, defence, astronomy, and scientific research. <sup>5–7</sup> However, the traditional materials used in terahertz devices no longer meet practical requirements, which has hindered related research progress.

Metamaterials, as a type of artificial composite material, replace the microscopic units of natural materials with artificial resonant units, exhibiting remarkable electromagnetic behaviors such as a negative index of refraction and electromagnetically induced transparency. Metamaterials have a strong response to electromagnetic waves, especially in terms of their absorption, reflection and transmission characteristics. They can effectively absorb electromagnetic waves in specific frequency bands and can be fabricated in smaller sizes while allowing for dynamic adjustment of electromagnetic wave absorption. The outstanding performance of metamaterials endows them with strong application potential in various frequency ranges such as microwave and terahertz

<sup>&</sup>lt;sup>a</sup>School of Physics and Optoelectronic Engineering, Yangtze University, Jingzhou, Hubei 434023, China. E-mail: hfzhang@yangtzeu.edu.cn

<sup>&</sup>lt;sup>b</sup>School of Mathematics and Science, Southwest University of Science and Technology, Mianyang 621010, China. E-mail: yizaomy@swust.edu.cn <sup>c</sup>School of Chemistry and Chemical Engineering, Jishou University, Jishou 416000, China

bands, and they are widely used in electromagnetically induced transparency, 11 microwave reception, 12 wireless energy transmission, 13 and hyperthermia technology. 14 Among the numerous metamaterials, Dirac semimetals have attracted the attention of researchers due to their excellent optical properties. 15-17 Dirac semimetals exhibit excellent response in the terahertz band, with typical examples including AlCuFe, Bi<sub>2</sub>Se<sub>3</sub>, and Na<sub>3</sub>Bi. 18,19 Unlike traditional semiconductor materials, Dirac semimetals can change their conductivity and dielectric constant by altering the bias voltage and doping of the alkaline surface, thereby enabling dynamic adjustment of the Fermi level.<sup>20</sup> The application of external electric and magnetic fields, as well as chemical doping, can significantly influence a material's conductivity, optical properties, and response to terahertz waves. This is particularly evident in the high tunability and adaptability of Dirac semimetals, enabling the design of efficient devices for broadband, narrowband, and dynamically adjustable absorbers.21 As one of the most common Dirac semimetals, AlCuFe quasicrystals have a high degeneracy factor and high electrical conductivity. Compared with most Dirac semimetals, they show better application potential. AlCuFe can be prepared by laser cladding, and the preparation process is already quite mature.<sup>22,23</sup>

The first metamaterial absorber membrane was designed and proposed by Landy et al. in 2008, 24 and since then, metamaterial absorbers have attracted increasing attention from researchers. Metamaterial absorbers can achieve both broadband and narrowband absorption. Broadband absorbers are often used in the design of filtering and stealth devices, while narrowband absorbers are commonly employed in the design of sensor devices.<sup>25</sup> The terahertz band possesses unique physical characteristics and broad application potential. Compared with traditional absorbers, metamaterial absorbers at terahertz frequencies can achieve more efficient energy absorption and have a wider range of applications in fields such as terahertz imaging, sensing, and detection. Researchers are gradually turning their attention to the study of metamaterial devices in the terahertz band. In 2008, Tao et al. from Boston University in the United States developed the first single-frequency narrowband absorber for the THz band by superimposing open rings and metal strip resonators, laying the foundation for the development of metamaterial absorbers in the terahertz band.<sup>26</sup> However, in the terahertz band, absorbers designed based on metals cannot dynamically adjust their absorption performance. To change the absorption performance of the absorber, it is necessary to redesign the structural parameters of the absorber, which is extremely laborintensive and costly. Researchers are gradually turning their attention to the study of absorbers that can be dynamically tuned. Later, the introduction of graphene solved this problem. As a two-dimensional material, graphene has a honeycomb lattice structure and exhibits excellent optical responses in the terahertz band. By changing the externally applied voltage, the Fermi level of graphene can be dynamically regulated. This characteristic enables the absorber with graphene to have excellent tunability.<sup>27</sup> However, graphene has

a zero or near-zero band gap, which limits its application in optical materials. 28,29 In 2012, Young et al. discovered that β-quartz BiO<sub>2</sub> can simulate graphene in three dimensions.<sup>30</sup> Since the bulk electrons of Dirac semimetals form a threedimensional Dirac-cone structure, the research on Dirac semimetals has gradually developed since then. The carrier mobility and the ability to resist the interference of the dielectric constant of Dirac semimetals are much higher than those of graphene, and Dirac semimetals can achieve more flexible control over electromagnetic energy.31 In 2013, Hu et al. proposed an absorber with four narrow-band high-absorption rates through full-wave electromagnetic simulation. This absorber is simple in design and has the advantage of being polarisation-insensitive. 32 In 2018, a tunable narrowband terahertz absorber was designed by Liu and his team; they combined Dirac semimetals with circular holes in a photonic crystal plate to achieve perfect absorption.<sup>33</sup> A Dirac semimetal-derived absorber operating across four bands was designed by Wu and colleagues in 2021, achieving over 95% absorption efficiency and 122 GHz  $RIU^{-1}$  sensitivity.<sup>34</sup> In 2025, Zhou *et al.* proposed a controllable perfect absorber by combining vanadium dioxide and Dirac semimetals. The absorption rate can be increased by 7.5% by changing the Fermi level and temperature. It exhibits peak sensitivity and FOM levels of 555 GHz RIU<sup>-1</sup> and 5, respectively, demonstrating excellent detection capabilities.35 An increasing number of studies indicate that BDS-based metamaterial absorbers at terahertz frequencies have entered a phase of accelerated development, demonstrating versatility in applications ranging from biomedical detection to precision sensing.

This paper proposes a four-band tunable absorber based on the Dirac semimetal AlCuFe quasicrystal, which exhibits polarisation insensitivity when electromagnetic waves are incident vertically because of the rotational symmetry of the absorber. In the 4-10 THz band, there were three absorption peaks above 97% and one above 94%. Through S-parameter inversion, the relative impedance of the structure was calculated, indicating that it complies with impedance matching theory. By decomposing and analysing the top-layer structure resonant cavity into blocks and performing a parametric scan analysis, the results obtained validated that the top-layer pattern and set parameters were the optimal design. At the same time, the physical mechanism of the absorber's operation was analysed using electric field analysis. The absorber exhibits good tunability through Fermi level modulation of the Dirac semimetal. By changing the refractive index of the external environment, analysis and calculation showed that the absorber has a high refractive index sensitivity, reaching up to 2800 GHz RIU<sup>-1</sup>, demonstrating excellent sensing performance. At the same time, the maximum quality factor Q value and figure of merit (FOM) value of the absorber were calculated to be 117.1 and 20.42, respectively. Collectively, these findings lead to the deduction that the designed device exhibits high selectivity and exceptional detection performance, showcasing wideranging applicability in diverse domains, including biomedical sensing, environmental detection, communication, and

**Paper Dalton Transactions** 

further research on related absorbers. This study also provides valuable references for future research.

#### Structural design and a single-cell 2. model

The design of a tunable absorber with sensing capabilities based on the Dirac semimetal AlCuFe quasicrystals at terahertz frequencies, as well as its top view and side view structures, is shown in Fig. 1. The absorber exhibits identical periodicity in both the X and Y directions. For a periodic unit, the unit side length is denoted as P. The periodic unit consists of three layers. From the top, electromagnetic waves are incident perpendicularly onto the absorber, inducing internal resonant phenomena.

The absorber's bottom layer is a gold substrate. Compared to Cu, Ag, and Al, Au exhibits higher reflectance stability, conductivity, and corrosion resistance.36-38 Let the thickness of Au be set as  $t_1$ , and the skin depth of terahertz waves in Au be  $\delta$ . Using the formula  $\delta = \sqrt{2/\omega\mu\sigma}$  to calculate the skin depth (where  $\omega = 2\pi f$ ,  $\mu$  is the permeability, and  $\sigma$  is the conductivity), we can set the thickness of the Au layer to be much greater than the skin depth of terahertz waves in Au, ensuring that the terahertz waves are completely absorbed and reflected, with no transmitted waves. 39,40 The intermediate dielectric layer is  $SiO_2$ , with its relative permittivity and thickness defined as  $\varepsilon$  = 1.56 and  $t_2$ , respectively. When the incident light enters the absorption layer from the top, a portion of the light is directly absorbed by the top layer, while the other part penetrates the top layer and enters the medium layer. The light propagates in the medium layer, reaches the bottom metal reflection layer and is reflected back. The reflected light meets the light just incident from the top layer. Under the condition of phase matching, constructive interference occurs, forming a strong localized electromagnetic field within the electric field, which causes the light to be absorbed. The top-layer structure pattern is shown in Fig. 1(b). At the centre of a square Dirac semimetal AlCuFe quasicrystal with side length P, a three-circle overlapping structure is etched, which can also be viewed as a resonant cavity formed by combining three two-third circles with

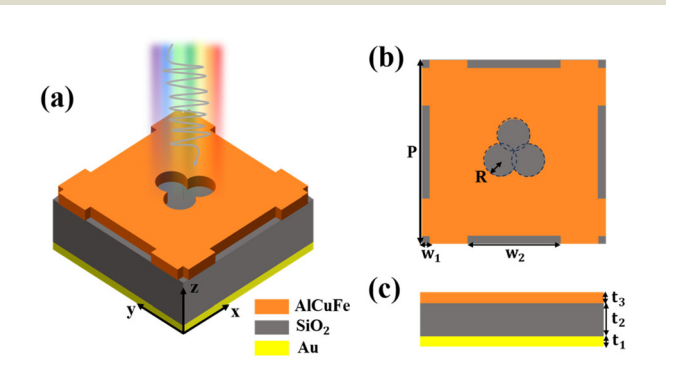


Fig. 1 Geometrical model of the absorber. (a) 3D view; (b) top view; and (c) side view.

radius R. Four square resonant cavities with side length  $w_1$  are etched at the four corners, and four rectangular resonant cavities with a width of  $w_1$  and a length of  $w_2$  are etched on each of the four sides. The top layer structure has a thickness of  $t_3$ . Simulation calculations were performed using CST simulation software,  $^{41-43}$  and the optimal parameters obtained were: P =42 μm,  $t_1$  = 0.25 μm,  $t_2$  = 12 μm,  $t_3$  = 1 μm,  $w_1$  = 1.2 μm,  $w_2$  = 16.6  $\mu$ m, and  $R = 2.3 \mu$ m. The AlCuFe quasicrystal's Fermi energy level  $E_{\rm F}$ , which is dynamically adjustable, was set to 80 meV. 15,16

The Kubo formula, applied within the random phase approximation (RPA) theory, allows for the derivation of the conductivity in AlCuFe quasicrystals:<sup>33</sup>

$$\operatorname{Re}\{\sigma(\Omega)\} = \frac{e^2}{\hbar} \frac{g k_{\rm F}}{24\pi} \Omega \theta(\Omega - 2) \tag{1}$$

$$\operatorname{Im}\{\sigma(\Omega)\} = \frac{e^2}{\hbar} \frac{g k_{\mathrm{F}}}{24\pi^2} \left\{ \frac{4}{\Omega} - \Omega \ln \left( \frac{4E_{\mathrm{c}}^2}{|\Omega^2 - 4|} \right) \right\}$$
 (2)

where the Fermi momentum is expressed as  $k_{\rm F} = E_{\rm F}/\hbar\nu_{\rm F}$ , and the Fermi velocity is expressed as  $\nu_{\rm F} \approx 10^6~{\rm m~s^{-1}}~\Omega = \hbar\omega/E_{\rm F}$  +  $i\hbar\tau^{-1}/E_{\rm F}$ , where  $\mu$  is the carrier mobility,  $\hbar\tau^{-1} = \nu_{\rm F}/(k_{\rm F}\mu)$ ,  $\tau = 4.5$  $\times$  10<sup>-13</sup> s,  $\varepsilon_{\rm c}$  =  $E_{\rm c}/E_{\rm F}$  ( $E_{\rm c}$  is the cutoff energy), the degeneracy factor is set to g = 40. The AlCuFe quasicrystal's dielectric constant can be obtained using a dual-band model and expressed as:31,34

$$\varepsilon = \varepsilon_{\rm b} + i\sigma/\omega\varepsilon_0 \tag{3}$$

where  $\varepsilon_0$  is the vacuum dielectric constant and the effective background dielectric constant is  $\varepsilon_b = 1$ .

We set the Fermi level of AlCuFe at 80 meV and used the MATLAB programming software to edit the dispersion relation of the complex dielectric constant of AlCuFe. Finally, the edited text file was imported into the CST software, and the unit and frequency range were set. The unit was set to µm, and the frequency range was set to 4-10 THz. Then, modeling was carried out. Periodic boundary conditions were set in the X and Y directions. In the Z direction, the incident wave was set as a Floquet port and an open boundary condition was applied. An adaptive tetrahedral mesh was adopted to enhance the accuracy of the numerical simulation. Subsequently, based on the finite element method, the CST software's frequency domain solver was utilized to calculate the S parameters of the model we designed. In the post-processing stage, the S parameters were substituted into the formula to calculate the absorber's absorption rate.44

In actual production, a series of processes can be used to prepare the entire absorber designed in this paper. The preparation flowchart is shown in Fig. 2. AlCuFe quasicrystals can be prepared using the laser melting method. The ultrapure elemental Al/Cu/Fe powder blends are injected into the laser focused area surrounded by high-concentration argon gas. Subsequently, a thin layer of powder melted by the laser beam was formed on the base, and after multiple scans, high-purity AlCuFe quasicrystals can be obtained. In addition, a gold layer was deposited on a single-crystal silicon wafer by electron

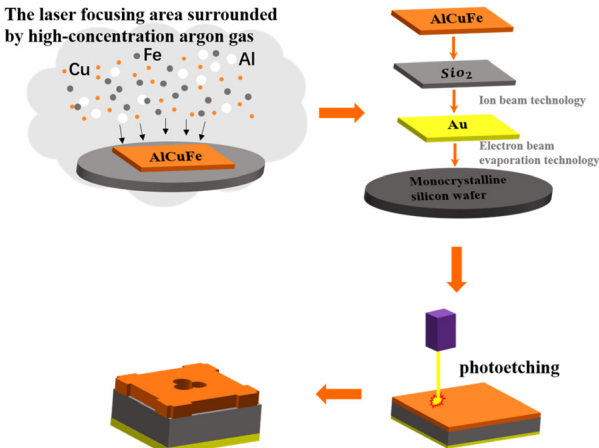


Fig. 2 Manufacturing process.

beam evaporation technology, and then a  $SiO_2$  layer was deposited on the gold substrate by ion beam technology. The prepared AlCuFe quasicrystal is deposited onto the  $SiO_2$  dielectric layer, and photolithography is used for etching to prepare an AlCuFe top layer film with a predetermined pattern, thereby completing the actual preparation of the entire device. 45–47

#### Results and discussion

The Au base layer, being much thicker than its skin depth, is sufficient to ensure that the transmittance of the absorber we designed is close to zero, with only reflection and absorption. S-parameters related to the absorber were calculated using CST software, where reflectance is  $R = |S_{11}|^2$  and transmittance is  $T = |S_{21}|^2$ . From the absorption rate A = 1 - T - R and since the transmittance T is close to zero, we know that  $A = 1 - R = 1 - |S_{11}|^2$ . Guided by the above theoretical research and computational analysis, we can obtain the absorption spectrum shown in Fig. 3(a). There are four perfect absorption peaks between 4 and 10 THz, labelled  $F_1$ ,  $F_2$ ,  $F_3$ , and  $F_4$ , with corresponding resonance frequencies of 4.99 THz, 6.138 THz, 7.846 THz, and 9.05 THz, and corresponding absorption rates of 97.4%, 94.7%, 97.9%, and 97.3%. According to the theory

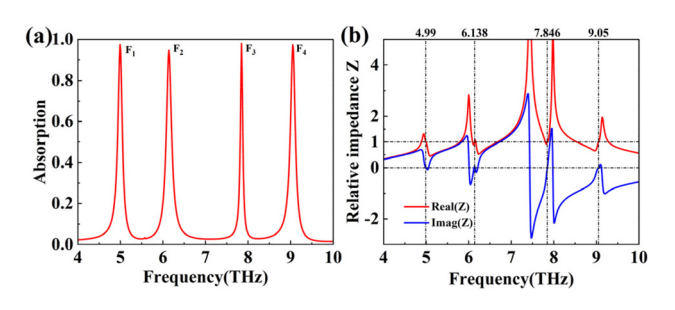


Fig. 3 (a) Absorption spectrum of the absorber and (b) schematic diagram of the equivalent impedance of the absorber within the operating range.

of impedance matching, the impedance of free space is 1.51 Achieving impedance matching between the absorber and free space  $(Z = Z_0)$  results in zero reflectance  $(R = |S_{11}|^2 = 0)$ , as shown in eqn (4), i.e., Z = 1, achieving impedance matching.52-54 According to equivalent circuit theory, the metamaterial structure is further equivalent to a circuit model. When the incident electromagnetic wave is perpendicular to the metamaterial device, the resonant unit will generate the corresponding induced surface current after interacting with the incident electromagnetic wave.<sup>55</sup> Based on the resonant effect between the resonant unit and the incident electromagnetic wave, the geometric and physical parameters of the structure are equivalent to circuit parameters, and the electromagnetic induction phenomenon generated when the electromagnetic wave is incident on the device is represented by the corresponding circuit components, for instance, the equivalent resistance R, equivalent inductance L, and equivalent capacitance C, whose values can be determined by the structural parameters and electromagnetic parameters of the metamaterial. Each layer of the metamaterial absorber is equivalent to a circuit load, with air and dielectric layers both being equivalent to transmission lines. The top metal pattern resonant layer is equivalent to an RLC series circuit. By paralleling the impedance of the metal pattern resonant layer and the surface impedance of the dielectric layer, the input impedance can be equivalently derived, that is, the equivalent impedance Z.56,57 Thus, it can be derived that the real and imaginary parts of the equivalent impedance of the absorber represented by Real(Z)and Imag(Z), respectively, can be obtained, and the reflection coefficient  $|S_{11}|$  can be expressed as eqn (4) and (5).

$$Z = \pm \sqrt{\frac{1 + S_{11}^2 - S_{21}^2}{1 - S_{11}^2 - S_{21}^2}} \tag{4}$$

$$|S_{11}| = \sqrt{\frac{Z - Z_0}{Z + Z_0}} = \sqrt{\frac{\left[\text{Real}(Z) - Z_0\right]^2 + \left[\text{Imag}(Z)\right]^2}{\left[\text{Real}(Z) + Z_0\right]^2 + \left[\text{Imag}(Z)\right]^2}}$$
 (5)

When the real part of the equivalent impedance Z, Real(Z) =  $Z_0$  = 1, and the imaginary part, Imag(Z) = 0,  $|S_{11}|$  = 0.<sup>58</sup> As shown in Fig. 3(b), the equivalent impedance diagram of the absorber is illustrated. At the corresponding absorption frequencies of the four absorption peaks, Real(Z) is close to 1, and the Imag(Z) is close to 0, satisfying impedance matching, perfect absorption is achieved in all four modes.

The physical mechanism of perfect absorption is elucidated through the electric field diagrams in the *xy* and *xz* directions under each resonance mode plotted in Fig. 4. By comparing Fig. 4(a)–(c), we can see that the electric fields at F<sub>1</sub>, F<sub>2</sub>, and F<sub>3</sub> are mainly concentrated within the rectangular frames along the *y*-axis. This originates from both the cavity resonance (CR) and the localized surface plasmon resonance (LSPR). Electromagnetic waves undergo multiple reflections and interference in a resonant cavity, converging their energy in the form of standing waves.<sup>59</sup> Through destructive interference, the energy of the electromagnetic waves is dissipated. At the same time, an electric field also converges on the lower

Paper **Dalton Transactions** 

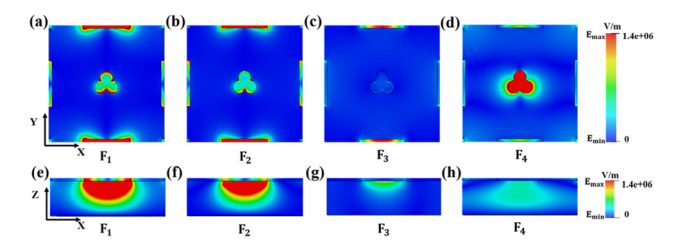


Fig. 4 (a)-(d) Electric field distribution in the xy direction for each resonance mode from  $F_1$  to  $F_4$ . (e)-(h) Electric field distribution in the xz direction for each resonance mode from F<sub>1</sub> to F<sub>4</sub>.

surface of the absorption layer, exciting localized surface plasmon polaritons between the upper AlCuFe layer and the SiO<sub>2</sub> layer. These plasmon polaritons resonate with incident electromagnetic waves at frequencies F<sub>1</sub>, F<sub>2</sub>, and F<sub>3</sub>, producing a localised surface plasmon polariton resonance effect, 60,61 which leads to an enhancement of the local surface field, thereby significantly enhancing the absorber's ability to capture and absorb electromagnetic waves. Similarly, dominated by CR and LSPR, in the F<sub>1</sub> and F<sub>2</sub> absorption modes, non-negligible electric fields were also generated in the edge rectangular resonator, the four-corner square resonator, and the central three-circle resonator in the x direction. As can be seen from Fig. 4(d), the electric field at F<sub>4</sub> is mainly concentrated in the three circular resonant cavities and is dominated by CR. By observing the electric field distribution in the xz direction in Fig. 4(e)-(h), most of the electric field in F<sub>1</sub> and F<sub>2</sub> is also captured by the dielectric layer. In addition to the local electric field generated at the interface of the absorbing and dielectric materials, the energy of the electromagnetic wave is dissipated through critical coupling via golden-ring resonance (GMR), 62,63 primarily depending on the propagation mode within the dielectric material, leading to localised enhancement of the electromagnetic wave rather than collective electron oscillations at the surface. Therefore, the strong electric fields observed in the dielectric layer within F<sub>1</sub> and F<sub>2</sub> are primarily dominated by GMR and LSPR.

In order to reveal the impact of the uppermost structure changes on the absorption performance of the absorber, two

sets of structural patterns were discussed. As shown in Fig. 5 and 6, case 4 is the control group. Fig. 5 discusses the different absorption performances of absorbers under different toplayer centre pattern structures. The structure of the top edge and four corners of the absorber remains unchanged, with only the centre-etched resonator undergoing changes from case 1 to case 4. As can be seen from the figure, when there is no resonant cavity at the centre of the top layer, as shown in case 1, only three absorption peaks F1, F2, and F3 are generated, with F3 having the lowest frequency. When circular resonant cavities are etched at the center of the top layer, as in cases 2 to 4, four absorption peaks appear in the absorption spectrum. When a circle is etched at the center, the central frequency of  $F_3$  is at 7.93 THz with an absorption rate of 74.5%, and the central frequency of F4 is at 9.456 THz with an absorption rate of 76.6%. When two circles are etched at the center, the central frequency of F<sub>3</sub> is at 7.8 THz with an absorption rate of 96.5%, and the central frequency of F4 is at 8.74 THz with an absorption rate of 82%. In case 4, three circles were etched at the center, resulting in four perfect absorption peaks. The central frequency of F3 was at 7.8 THz with an absorption rate of 97.9%, and the central frequency of F<sub>4</sub> was at 9.05 THz with an absorption rate of 97.3%. It can be seen that the number of circular resonators increases from one to three, the resonance of the resonators is enhanced, and the absorption peak undergoes a slight redshift, the absorption rates of F<sub>1</sub> and F<sub>2</sub> remained unchanged, while those of F<sub>3</sub> and F4 gradually increased. This proves that the central etching pattern we designed is the optimal structure. As shown in Fig. 6, we conducted further analysis and discussed the absorption effects produced by each part of the resonant cavity at the top layer of the designed absorber, In case 1, only the edge of the rectangular resonant cavity was etched, which had varying degrees of influence on F<sub>1</sub>-F<sub>4</sub>. As shown in Fig. 6(e), F<sub>1</sub> and F2 almost achieved perfect absorption under this resonant cavity, and the absorption rates of F3 and F4 reached 64.9% and 68.3%, respectively. As shown in Fig. 6(f), in case 2, the absorption rate of F<sub>4</sub> reached 79.1% when only the four-corner square resonant cavity was etched. It can be seen that the resonant cavity in case 2 plays a positive role in the absorption of the F<sub>4</sub> mode. Case 3 represents the resonant cavity with central

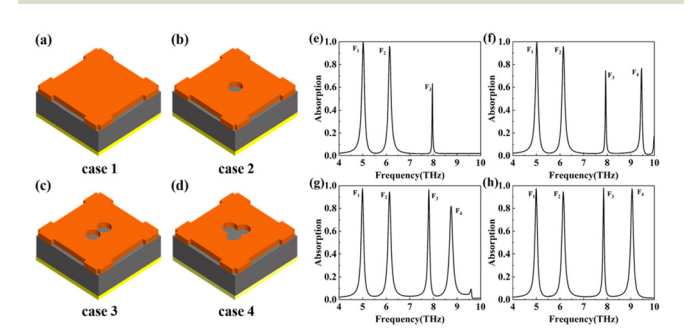


Fig. 5 (a)-(d) 3D diagrams of different centre structures at the top layer. (e)-(h) Absorption spectra of the absorbers corresponding to cases 1-4, respectively.

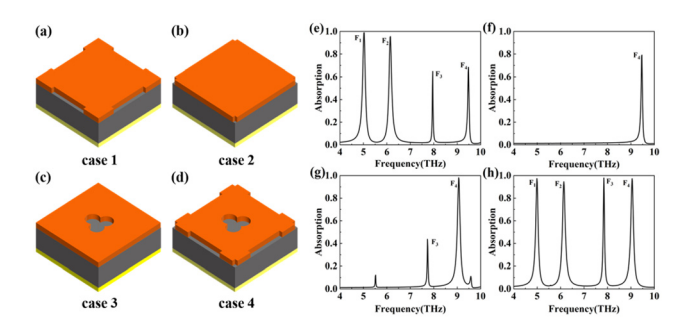


Fig. 6 (a)-(d) 3D diagrams of different top layer structures. (e)-(h) Absorption spectra of absorbers corresponding to cases 1-4, respectively.

etching, which is in line with the conclusion discussed in Fig. 5. It almost only affects F<sub>3</sub> and F<sub>4</sub>, with absorption rates reaching 43.6% and 98.1%, respectively. When case 2 and case 3 are superimposed on case 1, the absorption spectrum corresponding to case 4 demonstrates that F1 and F2 do not change significantly because they are mainly affected by case 1. F<sub>3</sub> and F<sub>4</sub> experience enhanced resonance due to the superposition of different resonant cavities, resulting in increased absorption rates and redshift. This improves overall absorption performance, achieving perfect absorption across four bands.<sup>64</sup> This discussion not only validates the rationality of the top-layer pattern we designed and explains the role of each part of the resonant cavity in producing different absorption peaks, but also shows that the superposition of resonances from different structural resonant cavities contributes positively to the absorption performance of the absorber.<sup>65</sup>

To further demonstrate the rationality, physical tuning, and tolerance of the structural parameters of the absorber designed in this paper, the control variable method was used to analyse some key parameters. In Fig. 7(a)-(g), the red curve represents the spectral diagram corresponding to the optimal parameter values of the device. In terms of physical tuning, it can be observed from Fig. 7(a) that as the radius R of the central circle increased from 1.9 µm to 2.7 µm, F4 experienced a significant redshift, with the frequency center shifting from 9.316 THz to 8.714 THz, and the absorption rate gradually increasing from 92.1% to 99.3%. F3 underwent a slight redshift, with the absorption rate gradually rising from 89.5% to 99.4% and then dropping to 98.6%. F1 and F2 showed almost no redshift or blueshift, but their absorption rates gradually decreased. Considering F1 to F4 as a whole, the parameters we set achieved the highest average absorption rate. In F<sub>1</sub> and F<sub>4</sub>, strong CR was observed in both rectangular cavities. During the process of increasing the radius R of the circle, the top microstructure changed, which weakened and strengthened the excitation effect of CR in the F<sub>1</sub> and F<sub>4</sub> modes, respectively, resulting in a gradual decrease and increase in the absorption rate of the F<sub>1</sub> and F<sub>4</sub> modes. In Fig. 7(b) and (c), the increase in  $w_1$  caused a noticeable blue shift in  $F_1$  and  $F_2$ , with the absorption rate corresponding to F1 gradually increasing and the absorption rate corresponding to F<sub>2</sub> gradually decreasing. In contrast to  $w_1$ , when  $w_2$  increased from 14.6  $\mu$ m to 18.6  $\mu$ m, both  $F_1$  and  $F_2$  exhibited significant red shifts. The absorption rate of F<sub>1</sub> gradually increased from 77.9% to 99.8%, while that of F2 decreased from 98.7% to 89.9%. This was due to the change in  $w_2$ , which led to the variation in the size of the BDS boundary. As a result, the LSPR and CR effects of the F1 and F2 modes within the rectangular resonant cavity were respectively enhanced and weakened. However, the main excitation regions of the F3 and F4 modes were different from those of the first two modes. Therefore, when  $w_1$  and  $w_2$  changed,  $F_3$  and  $F_4$ remained stable. When the cycle P was changed, as shown in Fig. 7(d), all four absorption peaks underwent a certain degree of redshift, and the corresponding absorption rates also changed to some extent. During the process where P increases from 41  $\mu$ m to 43  $\mu$ m, the absorption rate of F<sub>1</sub> rises from 95%

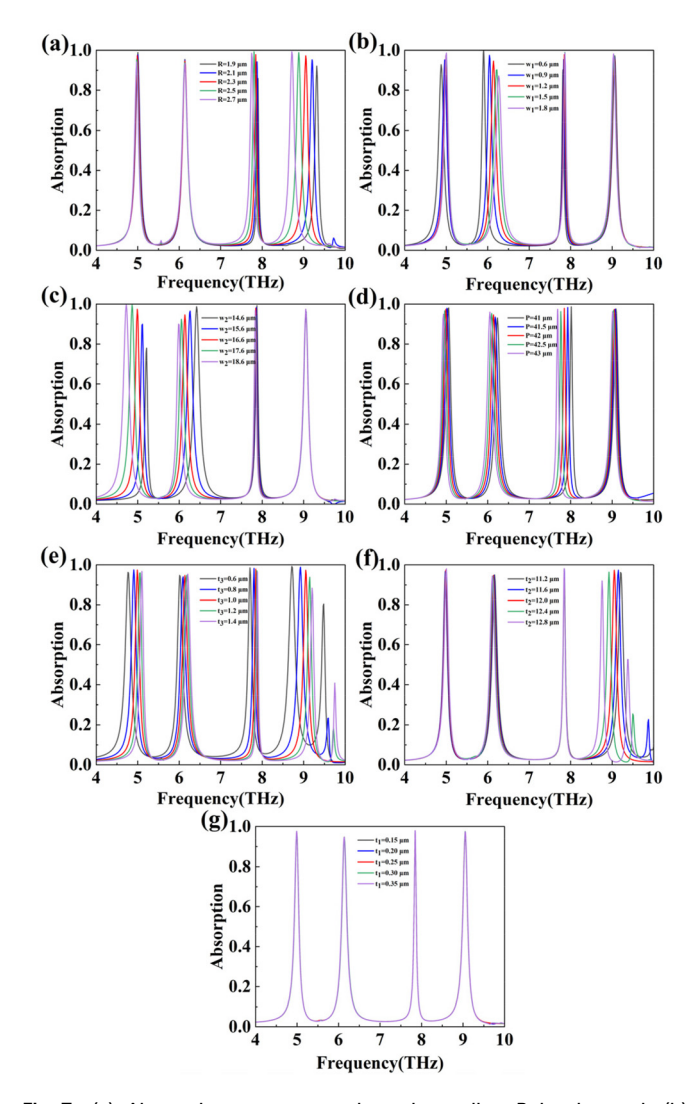


Fig. 7 (a) Absorption spectrum when the radius R is changed; (b) absorption spectrum when  $w_1$  is changed; (c) absorption spectrum when  $w_2$  is changed; (d) absorption spectrum when the period P is changed; (e) absorption spectrum when the thickness  $t_3$  of the AlCuFe layer is changed; (f) absorption spectrum when the thickness  $t_2$  of the dielectric layer is changed; and (g) absorption spectrum when the thickness  $t_1$  of the gold layer is changed.

to 98%, while that of F<sub>2</sub> drops from 96% to 93.1%. The absorption rate of F<sub>3</sub>, which was 97.4%, initially decreases to 96.3% and then continuously increases to 98.6%. The absorption rate of F<sub>4</sub> experiences a slight increase. The increase in P lengthens the oscillation period of the wave, which is beneficial for better absorption of electromagnetic waves. However, at the same time, the dimensions of each resonant cavity also increase, affecting the excitation effects of LSPR and CR. 66,67 These combined effects result in different changes in the absorption peaks under various modes. In Fig. 7(e), when the thickness  $t_3$  of the AlCuFe quasicrystalline layer was changed, all four absorption peaks shifted to a certain extent towards the blue end of the spectrum, and the corresponding changes in absorption rate were almost the opposite of the changes in the absorption rate when P was changed. In addition to analysPaper Dalton Transactions

ing changes in the absorption spectrum when the parameters of the absorption layer change, the impact of changes in the medium layer  $t_2$  on absorption performance was also discussed as shown in Fig. 7(f). When  $t_2$  increased from 11.2  $\mu$ m to 12.8 µm, only F4 underwent a noticeable red shift, with the absorption peak first increasing and then decreasing, its absorption rate increased from 96.2% to 97.3%, but then decreased to 92%, showing an overall downward trend. As shown in Fig. 7(g), when the thickness  $t_1$  of the bottom metal layer changes, the absorption spectrum graph remains almost unchanged, demonstrating that the bottom metal layer merely serves to prevent the electromagnetic wave from penetrating. This also indicates that under the condition where the thickness of the bottom metal layer is much greater than the skin depth, the bottom metal layer has excellent process tolerance in the actual manufacturing process. The above discussion demonstrates that the absorber has physical tuning capabilities, and that changes in different structural parameters have a significant impact on different absorption peaks. These results are highly consistent with the findings discussed earlier in this paper regarding the effects of different structural components of the top layer on different absorption peaks, further validating the correctness of the absorber's structural design.<sup>68</sup> At the same time, during the change process, the relatively stable absorption peak that does not change with the design parameters also reflects that the absorber has a certain tolerance.<sup>69</sup> During the process of changes in the absorption rate caused by parameter alterations, the parameters set in this paper exhibit the highest average absorption rate, indicating that the geometric dimensions of the device designed in this paper are reasonable. In summary, this indicates that the design of this absorber is reasonable and correct, and it has a certain degree of physical tuning and tolerance.

To investigate the stability of the absorber designed in this paper in actual complex electromagnetic environments, Fig. 8(a) and (b) discuss the changes in absorption performance under two polarisation modes and different electromagnetic wave incidence angles  $\theta$ , respectively. In this paper, the polarization directions of TE and TM correspond to the *X*-axis and *Y*-axis, respectively, and it can be seen in Fig. 8(a) that spectral absorption in both polarization configurations shows negligible discrepancies, demonstrating excellent polarisation

insensitivity. This is due to the unit structure of the absorber having a point-symmetric characteristic, which ensures that the absorber absorbs electromagnetic waves almost identically in different polarisation modes. 70,71 At the same time, as shown in Fig. 8(b), in the TE polarisation mode, F1 remains stable throughout the range of incident angles  $\theta$  from 0° to 70°, with the absorption rate consistently above 90%. Therefore, F<sub>1</sub> exhibits a certain degree of insensitivity to the angle of incidence and has strong adaptability, making it applicable to a variety of different electromagnetic environments. 72,73 However, with the incidence angle of electromagnetic waves progressively raised from 0° to 70°, the absorption rate of F3 gradually decreased to 0, and several unstable new absorption peaks appeared due to the continuous generation of new local fields around it. When  $\theta$  increases to more than 10°, F<sub>4</sub> gradually disappears and a new absorption peak appears due to membrane splitting. For  $F_2$ , as  $\theta$  increases from 0° to 25°, the absorption rate of F2 remains above 90%, but as  $\theta$  continues to increase, the absorption rate gradually decreases to approximately 40%, then gradually increases to 80%, and undergoes a certain amount of blue shift. Given the diverse changes exhibited by F<sub>1</sub>, F<sub>2</sub>, and F<sub>3</sub> at different incident angles, the absorber can be applied to certain studies with specific environmental requirements. In summary, absorbers can demonstrate a certain degree of stability and broad application potential in actual complex electromagnetic environments.

Considering the peculiar optical properties of Dirac semimetals, the  $E_{\rm F}$  of AlCuFe quasicrystals is controlled by chemical doping to regulate the absorption performance and explore the chemical tunability of the absorber. Fig. 9(a) shows the changes in the absorption spectrum as the  $E_{\rm F}$  of the Dirac semimetal changes from 70 meV to 90 meV. As  $E_{\rm F}$  increased, all four absorption peaks shifted towards blue, and the absorption rate changed but remained above 90%. The overall absorption rate was optimal at  $E_{\rm F}$  = 80 meV. Fig. 9(b) shows the displacement of each absorption peak as the Fermi level increases, which more intuitively illustrates that all four absorption peaks underwent a blue shift. This demonstrates the absorber's strong chemical tunability, enabling a wide range of applications in the field of sensing and detection.

The four-band narrowband absorber proposed in this paper is mainly used as a sensor component, and the key to evaluat-

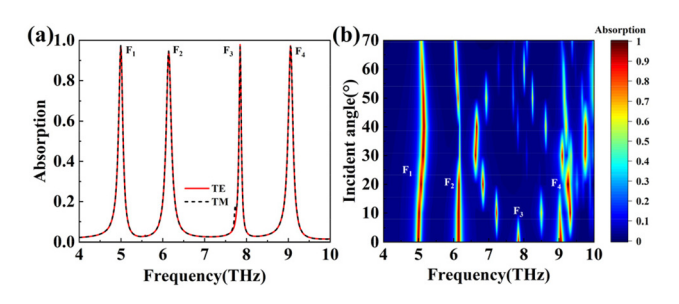


**Fig. 8** (a) Absorption spectra under different polarisation modes; (b) changes in the absorption rate in the TE mode when incident at different angles.

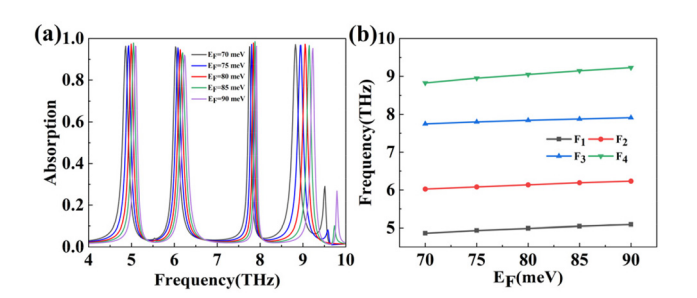


Fig. 9 (a) Absorption spectra of the AlCuFe quasicrystal at different Fermi levels. (b) Displacement changes of  $F_1-F_4$  in the AlCuFe quasicrystal at different Fermi levels.

ing the quality of a sensor component lies in the impact of changes in the external refractive index, n. As can be seen from the absorption spectrum in Fig. 10(a) when n changes from 1.00 to 1.15, all four absorption peaks underwent varying degrees of red shift, and the absorption rates of the four absorption peaks also underwent certain changes. Fig. 10(b) shows the displacement changes of F<sub>1</sub>-F<sub>4</sub> when n changes, clearly illustrating the varying degrees of red shifts of the four absorption peaks. For further analysis, the refractive index sensitivity S is used to intuitively describe the sensing performance of narrowband absorbers and is defined as:<sup>74</sup>

$$S = \Delta v / \Delta n \tag{6}$$

where  $\Delta v$  represents the change in the resonance frequency,  $\Delta n$  represents the change in the external refractive index, and

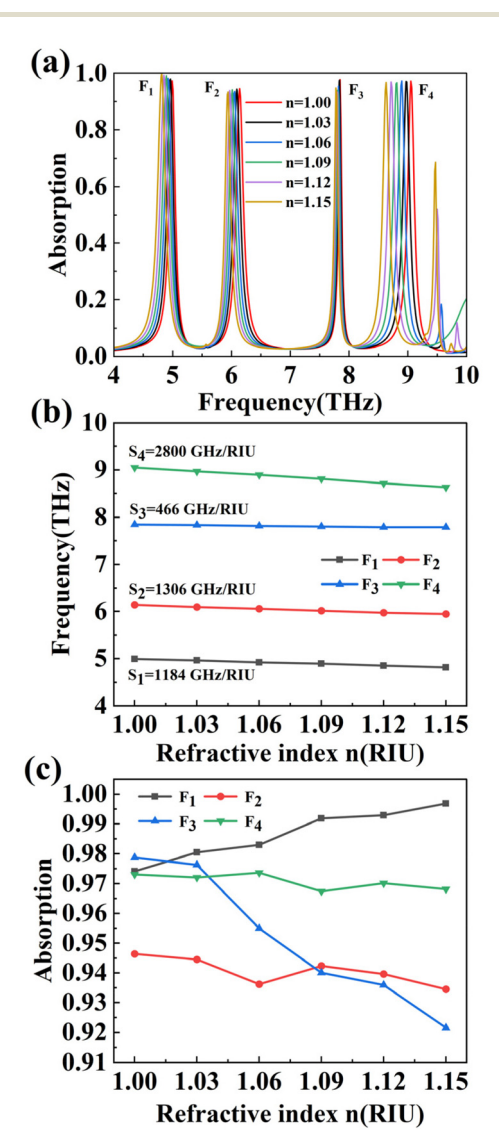


Fig. 10 (a) Absorption spectrum when the external refractive index changes; (b) displacement change diagram of F<sub>1</sub>-F<sub>4</sub> when the external refractive index changes; and (c) absorption rate change diagram of F<sub>1</sub>-F<sub>4</sub> when the external refractive index changes.

the larger the S value, the better the sensing performance. The absorption frequencies corresponding to F1-F4 at various refractive indices were organised and linear fitting based on formula (6) was performed to calculate the refractive index sensitivities S of  $F_1$ - $F_4$ , which are  $S_1 = 1184$  GHz  $RIU^{-1}$ ,  $S_2 = 1306$ GHz RIU<sup>-1</sup>,  $S_3 = 466$  GHz RIU<sup>-1</sup>, and  $S_4 = 2800$  GHz RIU<sup>-1</sup>, respectively. Among these, the highest refractive index sensitivity reached 2800 GHz RIU<sup>-1</sup>, demonstrating excellent sensing performance and offering significant application advantages in relevant detection fields. As shown in Fig. 10(c), the change in the refractive index n affects the absorption rates of each absorption peak. As n increases, the absorption rates of F2 and F4 continuously increase and decrease, respectively, while the absorption rate of F<sub>1</sub> steadily increases and that of F<sub>3</sub> decreases significantly, the absorption rates of F1-F4 remain above 90% throughout.

In addition, we summarize the important parameter values under each absorption mode in Table 1 to facilitate a more intuitive understanding of the relevant performance of the absorber. Among them, the Q value used to evaluate the high selectivity of the absorber and the FOM value used to evaluate the sensing performance are calculated using eqn (7) and (8), respectively. 15,17,62,75

$$Q = f_0 / \text{FWHM} \tag{7}$$

$$FOM = S/FWHM \tag{8}$$

Here, FWHM refers to the width of the absorption peak at half of the maximum absorption rate, and  $f_0$  represents the central wavelength. The maximum Q value of the absorber is 117.1, and the maximum FOM value is 20.42. This demonstrates the high selectivity and good sensing performance of the absorber, showing certain application potential in the fields of sensing and detection.

In Table 2, a comparison was made between the designed four-band narrowband absorber and the narrowband absorbers reported in recent years. For instance, the absorber we designed has the same number of layers as those in ref. 75 and 76, but it exhibits more absorption peaks and a greater refractive index sensitivity S and also features a more convenient voltage tuning method. The absorber described in this paper has certain advantages in terms of structural design and tunability, and its high sensitivity makes it widely applicable in the fields of biosensing and environmental detection. It also provides insights into research on Dirac semimetal functional devices in the THz band.

Table 1 The absorption rate, central frequency, Q value, FOM value and refractive index sensitivity of the absorber in F<sub>1</sub>-F<sub>4</sub> modes

	Absorption	$f_0$ (THz)	FWHM (THz)	Q	FOM	S (GHz RIU <sup>-1</sup> )
$\mathbf{F_1}$	97.4%	4.99	0.1251	39.87	9.47	1184
$F_2$	94.7%	6.138	0.1489	41.24	8.77	1306
$\mathbf{F}_3$	97.9%	7.846	0.067	117.1	6.96	466
$F_4$	97.3%	9.05	0.1371	66	20.42	2800

Table 2 Comparison between absorbers reported in recent years and the absorb	ser designed in this paper
--	----------------------------

Ref.	Number of peaks	f peaks Wave band (THz) Tunable material Frequency modulation method		Layers	S (GHz RIU <sup>-1</sup> )	
75	2	0.8-1.4	Metal	Structure	3	37
76	4	0-1.1	Graphene	Voltage	14	50
77	5	0.3-2.5	BDS	Voltage	3	134.75
78	1	1.0-2.2	Metal	Structure	3	300
79	3	2-5	Graphene	Voltage	2	1080
80	3	3.4-5.2	BDS	Voltage	3	405
Proposed	4	4-10	BDS	Voltage	3	2800

#### 4. Conclusions

This paper presents the design of a four-band tunable absorber based on AlCuFe quasicrystals at terahertz frequencies. The absorber exhibits four absorption peaks F<sub>1</sub>-F<sub>4</sub>, with three peaks showing absorption rates above 97% and one peak with an absorption rate above 94% in the 4-10 THz band. By calculating the equivalent impedance of the absorber, it is demonstrated that it complies with impedance matching theory, thereby achieving perfect absorption. Furthermore, by analysing the generation and distribution of electric fields, the physical mechanism by which the absorber achieves perfect absorption is explained. The effect and influence of the top microstructure on the four absorption peaks were discussed in detail. Subsequently, by changing the structural parameters, we further confirmed the rationality, physical tuning, and tolerance of our designed absorber. By utilising the unique optical properties of AlCuFe quasicrystals and altering the Fermi level, the excellent chemical tunability of the absorber is explained. Considering the actual situation, the angle of electromagnetic wave incidence was changed to study the resulting changes in absorption performance, and it was found that F1 and F2 exhibit good adaptability to complex actual environments. Finally, the changes in the absorption spectrum due to changes in the external refractive index are used to intuitively measure the quality of the absorber as a sensor component using refractive index sensitivity S, with a maximum S of up to 2800 GHz  $RIU^{-1}$ . In comparison with some recently reported studies, the absorber designed in this paper shows obvious advantages in many aspects. In summary, this device exhibits excellent performance, providing ideas for related absorbers and further research, and has great application potential in the field of sensing and detection.

#### Conflicts of interest

There are no conflicts to declare.

## Data availability

All data presented in this study are displayed in the figures of this paper. The original datasets are available from the corresponding author upon reasonable request.

### Acknowledgements

The authors are grateful to the National Natural Science Foundation of China (No. 12074151) for the support.

#### References

- H. T. Chen, W. J. Padilla, J. M. O. Zide, A. C. Gossard,
   A. J. Taylor, et al., Nature, 2006, 444(7119), 597–600.
- 2 S. J. Zhang, T. Cao and Z. Tian, *Opto-Electron. Eng.*, 2023, 50(9), 230142.
- 3 J. X. Fan, Z. L. Li, Z. Q. Xue, H. Y. Xing, D. Lu, et al., Opto-Electron. Sci., 2023, 2, 230006.
- 4 N. V. Chernomyrdin, G. R. Musina, P. V. Nikitin, I. N. Dolganova, A. S. Kucheryavenko, *et al.*, *Opto-Electron. Adv.*, 2023, **6**, 220071.
- 5 W. X. Li, Y. T. Yi, H. Yang, S. B. Cheng, W. X. Yang, H. F. Zhang, Z. Yi, Y. G. Yi and H. L. Li, *Commun. Theor. Phys.*, 2023, 75, 045503.
- 6 Q. F. Ma, J. L. Ren, X. F. Sun, S. F. Wang, X. J. Chen, G. R. Liu and H. Yang, *Chem. Eng. J.*, 2025, **509**, 161444.
- 7 J. Zhao, H. R. Lai and M. Li, *Int. J. Miner.*, *Metall. Mater.*, 2025, 32, 619–630.
- 8 B. W. Liu and F. Chen, Phys. B, 2025, 714, 417423.
- 9 X. Ning, T. Y. Sun, Q. J. Song, Z. Yi, S. B. Cheng, J. Q. Wang, Q. D. Zeng and Y. G. Yi, *Commun. Theor. Phys.*, 2025, 77, 095702.
- 10 Y. B. Zhang, Z. Yi, X. Y. Wang, P. X. Chu, W. T. Yao, Z. G. Zhou, S. B. Cheng, Z. M. Liu, P. H. Wu, M. Pan and Y. G. Yi, *Phys. E*, 2021, 127, 114526.
- 11 B. X. Wang, G. Duan, W. Lv, Y. Tao, H. Xiong, D. Q. Zhang, G. Yang and F. Z. Shu, *Nanoscale*, 2023, 15(45), 18435–18446.
- 12 Q. Yang, H. Xiong, J. H. Deng, B. X. Wang, W. X. Peng, et al., Appl. Phys. Lett., 2023, 122, 253901.
- 13 H. Xiong, Q. Yang, Y. Z. Huang, J. H. Deng, B. X. Wang and H. Q. Zhang, ACS Appl. Mater. Interfaces, 2024, 16(44), 60189-60196.
- 14 H. Xiong, J. Y. Xie, Y. J. Liu, B. X. Wang, D. P. Xiao and H. Q. Zhang, *Adv. Funct. Mater.*, 2025, 35(1), 2411842.
- 15 L. Y. Li and F. Chen, Phys. Lett. A, 2025, 544, 130489.
- 16 B. W. Zhang and Y. N. Luo, Phys. Lett. A, 2025, 541, 130419.
- 17 Z. L. Zeng, H. F. Li, H. F. Zhang, S. B. Cheng, Y. G. Yi, Z. Yi, J. Q. Wang and J. G. Zhang, *Photonics Nanostruct. Fundam. Appl.*, 2025, 63, 101347.

- 18 S. B. Cheng, W. X. Li, H. F. Zhang, M. N. Akhtar, Z. Yi, Q. D. Zeng, C. Ma, T. Y. Sun, P. H. Wu and S. Ahmad, Opt. Commun., 2024, 569, 130816.
- 19 Z. Y. Chen, S. B. Cheng, H. F. Zhang, Z. Yi, B. Tang, J. Chen, J. G. Zhang and C. J. Tang, Phys. Lett. A, 2024, 517, 129675.
- 20 X. Y. Tang and F. Chen, Micro Nanostruct., 2025, 207, 208265.
- 21 J. X. Jiang, Y. T. Yi, Q. J. Song, Z. Yi, C. Ma, Q. D. Zeng, T. Y. Sun, S. B. Cheng, Y. G. Yi and M. N. Akhtar, Phys. E, 2025, 165, 116123.
- 22 Z. Li, Y. Pan, F. Chen and W. X. Yang, Micro Nanostruct., 2025, 204, 208156.
- 23 W. Q. Lu, Y. T. Yi, Q. J. Song, Z. G. Zhou, Y. G. Yi, Q. D. Zeng and Z. Yi, Acta Phys. Sin., 2025, 74(3), 034101.
- 24 N. I. Landy, S. Sajuyigbe, J. J. Mock, D. R. Smith and W. J. Padilla, Phys. Rev. Lett., 2008, 100(20), 207402.
- 25 W. Yang and Y. S. Lin, Opt. Express, 2020, 28(12), 17620-17629.
- 26 H. Tao, N. I. Landy, C. M. Bingham, X. Zhang, R. D. Averitt and W. J. Padilla, Opt. Express, 2008, 16(10), 7181-7188.
- 27 Z. Li, Q. Song, L. Jia, Z. Yi, S. Cheng, J. Wang and B. Li, Opt. Commun., 2025, 583, 131768.
- 28 P. Wang, M. Yang, S. Tang, Y. Li, X. Lin, H. Zhang, Z. Zhu and F. Chen, J. Alloys Compd., 2022, 918, 165607.
- 29 Z. Ai, H. F. Liu, S. B. Cheng, H. F. Zhang, Z. Yi, Q. D. Zeng, P. H. Wu, J. G. Zhang, C. J. Tang and Z. Q. Hao, J. Phys. D: Appl. Phys., 2025, 58, 185305.
- 30 S. M. Young, S. Zaheer, J. C. Y. Teo, C. L. Kane, E. J. Mele, et al., Phys. Rev. Lett., 2012, 108(14), 140405.
- 31 T. Liang, Q. Gibson, M. N. Ali, M. Liu, R. J. Cava and N. P. Ong, Nat. Mater., 2015, 14, 280-284.
- 32 F. Hu, L. Wang, B. Quan, X. Xu, Z. Li, Z. Wu and X. Pan, J. Phys. D: Appl. Phys., 2013, 46(19), 195103.
- 33 G. D. Liu, X. Zhai, H. Y. Meng, Q. Lin, Y. Huang, C. J. Zhao and L. L. Wang, Opt. Express, 2018, 26(9), 11471-11480.
- 34 X. Wu, Y. Zheng, Y. Luo, J. Zhang, Z. Yi, X. Wu, S. Cheng, W. Yang, Y. Yu and P. Wu, Phys. Chem. Chem. Phys., 2021, **23**(47), 26864–26873.
- 35 J. Zhou, S. Wu, K. Jin, Y. He, X. Yang and J. Xu, Alexandria Eng. J., 2025, 116, 104-111.
- 36 J. Zhao, H. Junkun, Z. Min, S. Hong, L. Ling, et al., Opto-Electron. Eng., 2023, 50(9), 230140.
- 37 F. L. Cao and B. J. Chen, Knowl.-Based Syst., 2019, 178, 98–110.
- 38 J. L. Ren, Q. F. Ma, X. F. Sun, J. Y. Ma, G. R. Liu and H. Yang, Fuel, 2025, 397, 135454.
- 39 H. Xiong, X. D. Ma, H. S. Liu, D. P. Xiao and H. Q. Zhang, Appl. Phys. Lett., 2023, 123(15), 153902.
- 40 Z. Yi, J. K. Li, J. C. Lin, F. Qin, X. F. Chen, W. T. Yao, Z. M. Liu, S. B. Cheng, P. H. Wu and H. L. Li, Nanoscale, 2020, 12, 23077.
- 41 W. X. Li, S. B. Cheng, Z. Yi, H. F. Zhang, Q. J. Song, Z. Q. Hao, T. Y. Sun, P. H. Wu, Q. D. Zeng and R. Raza, Appl. Phys. Lett., 2025, 126, 033503.
- 42 X. W. Jiang, T. H. Yan, J. J. Zhu, B. He, W. H. Li, H. P. Du, et al., Cogn. Comput., 2020, 12, 979-990.

- 43 L. Liu, W. Liu, Q. Liu, Y. Chen, X. Yang, Y. Zhang and Z. Yi, Coatings, 2025, 15, 856.
- 44 Z. Wang, W. Pan, Y. He, Z. Zhu, X. Jin, M. Liu, S. Ma, Q. He, S. Sun and L. Zhou, Opto-Electron. Sci., 2025, 4, 240024.
- 45 Y. Z. Huang, O. Yang, H. Xiong and H. O. Zhang, Appl. Phys. Lett., 2025, 126, 063901.
- 46 G. R. Liu, Y. Y. Dai, X. F. Sun, J. Y. Ma, T. Xian and H. Yang, Sep. Purif. Technol., 2025, 361, 131622.
- 47 Y. Y. Dai, G. R. Liu, X. F. Sun, J. Y. Ma, T. Xian and H. Yang, Appl. Surf. Sci., 2025, 681, 161611.
- 48 H. Hu, F. Chen, Y. Li, J. Li, L. Cui, D. Jiang, X. Lin and J. Gao, J. Alloys Compd., 2025, 1024, 180216.
- 49 J. Wang, M. S. Liu, H. Yang, Z. Yi, C. J. Tang, J. Deng, J. Q. Wang and B. X. Li, Opt. Commun., 2025, 132415, DOI: 10.1016/j.optcom.2025.132415.
- 50 J. Zhao, Y. X. Lu and Z. Zhou, Comput. Electr. Eng., 2020, 86, 106757.
- 51 H. Sun, Z. Yi, C. Ma, S. B. Cheng, B. Tang, Q. D. Zeng and S. Ahmad, Commun. Theor. Phys., 2024, 76(7), 075701.
- 52 J. Wang, H. Yang, Z. Yi, J. Wang, S. Cheng, B. Li and P. Wu, Photonics, 2025, 12(5), 451.
- 53 X. Guo, C. Tang, Z. Yi, S. Cheng, J. Wang and B. Li, Curr. Appl. Phys., 2025, 76, 16-25.
- 54 Y. Zheng, Z. Y. Wang, Q. J. Song, Z. Yi, S. B. Cheng, C. Ma, C. J. Tang, Q. D. Zeng and S. Ahmad, Commun. Theor. Phys., 2024, 77(1), 015702.
- 55 J. Hu, Z. Y. Tang, X. Lan, Q. R. Deng, W. T. Zhang, Y. J. Huang and L. Li, Opto-Electron. Eng., 2023, 50(8), 220284.
- 56 Y. Yuan, H. F. Liu, M. S. Liu, W. B. Zhang, X. H. Li and S. B. Cheng, Phys. Lett. A, 2025, 556, 130832.
- 57 S. H. Liu and F. Chen, Phys. B, 2025, 715, 417638.
- 58 H. Han, J. Zhao, W. Zhai, Z. Xiong, D. Niyato, M. Di Renzo, Q. V. Pham, W. Lu and K. Y. Lam, IEEE Trans. Commun., 2021, 69, 7821-7836.
- 59 W. X. Li, S. B. Cheng, H. F. Zhang, Z. Yi, B. Tang, C. Ma, P. H. Wu, Q. D. Zeng and R. Raza, Commun. Theor. Phys., 2024, 76, 065701.
- 60 W. F. Fu, Z. Y. Wang, Z. Yi, Q. J. Song, L. Bian, S. B. Cheng, B. Tang, T. Y. Sun, G. F. Li and S. Ahmad, Phys. B, 2024, 677, 415708.
- 61 X. F. Sun, J. Q. Zhang, M. X. Luo, J. Y. Ma, T. Xian, G. R. Liu and H. Yang, Chem. Eng. J., 2024, 499, 156455.
- 62 X. Z. Yang, Q. J. Song, C. Ma, Z. Yi, S. B. Cheng, B. Tang, C. Liu, T. Y. Sun and P. H. Wu, Phys. E, 2024, 161, 115954.
- 63 Q. F. Ma, J. L. Ren, X. F. Sun, X. J. Chen, G. R. Liu, S. F. Wang and H. Yang, Appl. Surf. Sci., 2025, 679, 161275.
- 64 P. Chen, Y. T. Yi, Q. J. Song, Z. Yi, Y. G. Yi, S. B. Cheng, J. G. Zhang, C. J. Tang, T. Y. Sun and Q. D. Zeng, Photonics, 2024, 11(7), 604.
- 65 Z. Ai, Y. T. Yi, H. Yang, M. S. Liu, Y. G. Yi, C. J. Tang and F. Gao, Phys. Lett. A, 2025, 556, 130827.
- 66 X. Huang, Y. T. Yi, Q. J. Song, Z. Yi, C. Ma, C. J. Tang, Q. D. Zeng, S. B. Cheng and R. Raza, Commun. Theor. Phys., 2024, 76(11), 115702.

**Paper** 

67 X. C. Yao, Z. Yi, C. Liu, J. G. Zhang, S. B. Cheng, Q. D. Zeng, J. Chen, Y. G. Yi and C. J. Tang, *Opt. Commun.*, 2024, 570, 130937.

- 68 H. F. Liu, J. J. Li, H. Yang, J. Q. Wang, B. X. Li, H. Zhang and Y. G. Yi, *Photonics*, 2025, **12**(5), 443.
- 69 X. F. Sun, T. Xian, C. Y. Sun, J. Q. Zhang, G. R. Liu and H. Yang, *J. Mater. Sci. Technol.*, 2025, **228**, 256–268.
- 70 Y. Liu, M. Liu, H. Yang, Z. Yi, H. Zhang, C. Tang, J. Deng, et al., Phys. Lett. A, 2025, 552, 130653.
- 71 X. Wang, Z. Zhang, J. Li, Y. Wang, H. Cao, Z. Li and L. Shan, *J. Wirel. Commun. Netw.*, 2019, **193**, 2019.
- 72 J. L. Ren, Q. F. Ma, X. F. Sun, S. F. Wang, G. R. Liu, H. Yang and J. Colloid, *Interface Sci.*, 2025, **691**, 137452.
- 73 Z. T. Li, S. B. Cheng, H. F. Zhang, W. X. Yang, Z. Yi, Y. G. Yi, J. Q. Wang, S. Ahmad and R. Raza, *Phys. Lett. A*, 2025, 534, 130262.

- 74 T. T. Dai, Y. T. Yi, Z. Yi, Y. J. Tang, Y. G. Yi, S. B. Cheng, Z. Q. Hao, C. J. Tang, P. H. Wu and Q. D. Zeng, *Photonics*, 2024, 11(9), 784.
- 75 D. Wang, K. D. Xu, S. Luo, Y. Cui, L. Zhang and J. Cui, *Nanoscale*, 2023, **15**(7), 3398–3407.
- 76 Z. Bao, J. Wang, Z. D. Hu, Y. Chen, C. Zhang and F. Zhang, J. Phys. D: Appl. Phys., 2021, 54(50), 505306.
- 77 X. Qin, J. Jiang, G. Duan, C. Xu, X. Zhang, H. Zhu, Y. Huang, N. Xu and B. X. Wang, *J. Opt.*, 2024, 26(4), 045103.
- 78 A. S. Saadeldin, M. F. O. Hameed, E. M. A. Elkaramany and S. S. A. Obayya, *IEEE Sens. J.*, 2019, **19**(18), 7993–7999.
- 79 J. H. Ge, C. You, H. Feng, X. Li, M. Wang, L. Dong, G. Veronis and M. Yun, *Opt. Express*, 2020, **28**(21), 31781–31795.
- 80 W. Zhou, X. Qin, Y. Chen, Q. Zhao, Y. Huang, H. Zhou, N. Xu and B. X. Wang, J. Opt. Soc. Am. B, 2024, 41(10), 2318–2327.